Coaxial Multiphase Flame for Continuous-Flow Assembly of Ternary Nanocomposite Photocatalysts

Bongseop Kwak, Jungwook Choi,* Jiseok Lim,* and Jeong Hoon Byeon*

For the low-cost production of graphene (G)-included composites, the growth of graphene on a transition metal in hydrocarbon flames is introduced, where the hydrocarbons are adsorbed on the metal surface, followed by catalytic decomposition, leading to continuous G formation. On the other hand, the flame synthesis of G is still a batch process, limiting the practical applications of such materials. Moreover, the hybridization of G for enhanced catalytic activities requires additional reaction and separation steps. Here, a coaxial multiphase flame is generated and combined with a rotating Cu–Ni foil and ultrasonic bath for the continuous-flow assembly of ternary G composites with low-cost and rapid implementation. The continuous flows to generate a multicomponent flame consist of MoS_2 particle-laden N_2 gas (inner), titanium isopropoxide vapor-laden CH_4-air (middle), and ethanol liquid (outer), while Cu–Ni foil plies between the flame and ultrasonic bath for the assembly and dispersion of MoS_2–TiO_2@G composites. The configuration of the composite can be modulated by replacing the MoS_2 flow with a CdS flow to construct CdS–TiO_2@G. From photocatalytic H_2 production and CO_2 reduction tests, the developed coaxial flame provides comparable performance with analogous architectures from the usual multistep methods despite the high-throughput production.

1. Introduction

According to the critical issues in energy supply and global warming such as H_2 production and CO_2 reduction,[1] developing advanced photocatalysis is strongly encouraged to provide a long-term solution and has been progressed significantly using nanoscale composites containing semiconductor photocatalysts (e.g., titanium dioxide (TiO_2) and zinc oxide (ZnO)), quantum dots as cocatalysts (e.g., molybdenum disulfide (MoS_2) and cadmium sulfide (CdS)), and carbonaceous nanosheets as highly conductive and large surfaces (e.g., graphenes (G) and graphitic carbon nitrides) owing to their advantageous combined properties for prolonging the lifetime of photogenerated electrons.[2–5] Specifically, the incorporation of MoS_2–TiO_2 (or CdS–TiO_2) hybrids onto G nanosheets as surface engineering was recently investigated to suppress the rapid charge recombination from the multipoint electron transfers between the individual components for securing optimal photocatalytic performance,[6–10] which boosts the kinetics and stability in H_2 production and CO_2 reduction compared to those of the singular or binary photocatalysts without G nanosheets.[11–14]

The typical noncontinuous preparation methods of G-containing composite photocatalysts for energy and environmental applications usually involve vacuum vapor deposition or multistep hydrothermal reactions as well as pre- and post-treatments.[15,16] Combining the multiple functional components on G nanosheets for enhancing their photocatalytic performance complicates their preparation because they increase the number of treatments, which include additional controls.[17] Moreover, the high production cost from vacuum processes and multiple chemistries may require alternative strategies for the mass production of these composites.[15,18] These trade-offs may limit the utilization of the composite photocatalysts to be used in practical energy and environmental applications because developing optimal manufacturing processes still require large investments and research efforts to examine their effectiveness.[1,9,19,20]

On this account, several studies used flame aerosol synthesis (FAS) for the scalable production of semiconductor photocatalytic materials because FAS requires fewer preparation steps and generates less wastes. Moreover, it can be a viable option for the large-scale manufacturing of nanoscale catalysts from low-cost sources.[21,22] On the other hand, most FAS strategies focus mainly on producing singular or binary metallic nanoparticles through the pyrolysis and subsequent oxidation of precursors at high temperatures to accelerate the nucleation and condensation of pyrolyzed precursors,[23,24] even though it is even affordable for the production of G nanosheets in a
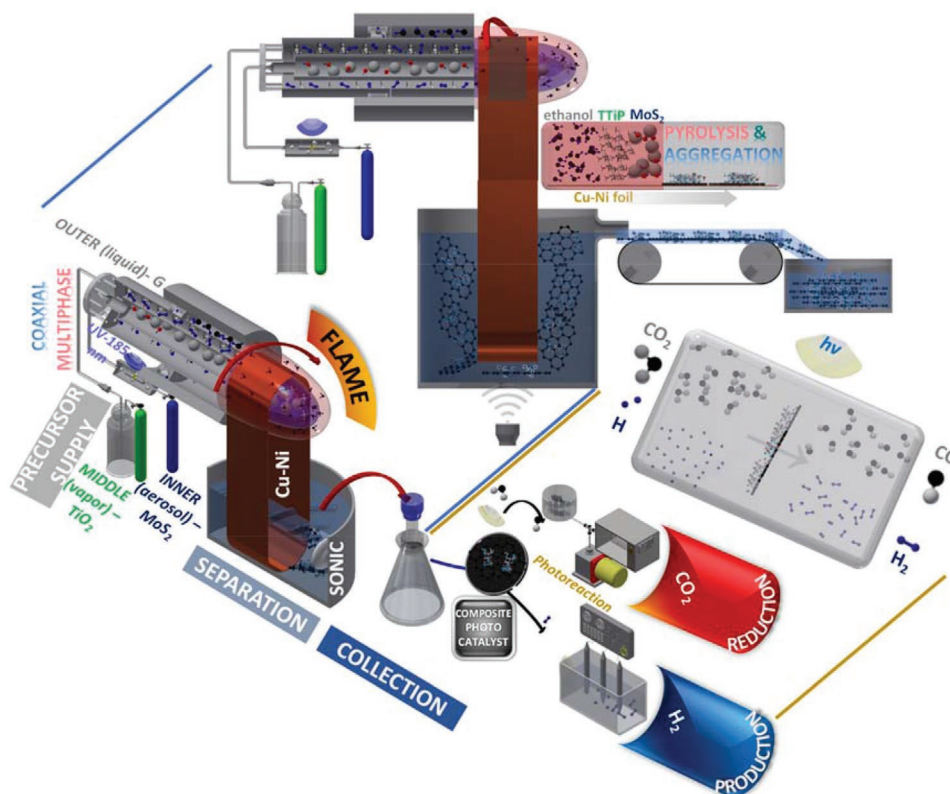
B. Kwak
College of Medicine
Dongguk University
Goyang 10326, Republic of Korea

J. Choi
School of Mechanical Engineering
Chung-Ang University
Seoul 06974, Republic of Korea
E-mail: choij@cau.ac.kr

J. Lim, J. H. Byeon
School of Mechanical Engineering
Yeungnam University
Gyeongsan 38541, Republic of Korea
E-mail: jlim@yu.ac.kr; postjb@yu.ac.kr

Figure 1. Schematic diagram of the coaxial multiphase flame used to assemble the G-included ternary nanocomposites for H_2 production and CO_2 reduction. The flame was integrated with a rotating Cu–Ni foil and ultrasonic probe inserted bath for the formation and collection of the resulting composites. The flows for multiphase flame consisted of MoS_2 (or CdS)-laden N_2 (inner), TTIP vapor-laden CH_4-air (middle), and liquid ethanol (outer) for the catalytic growth of G and the subsequent deposition of MoS_2 (or CdS) and TiO_2 particles on a rotating Cu–Ni foil. The resulting materials on the rotating foil were immersed in an ultrasonic bath to detach and disperse them subsequent spray drying and collection (refer to the upper-left detailed scheme). The resulting MoS_2–TiO_2@G or (CdS–TiO_2@G) composites were placed in photoreactors to determine the H_2 production and CO_2 reduction performance (refer to the upper-right detailed scheme).

single-pass configuration unlike the preparations based on vacuum vapor deposition and the Hummers' method.[25–27]

Therefore, in this study, an aerosol single-pass prototype was developed for low-cost, fast implementation, and mass production, including the reconfigurable assembly of ternary nanocomposites by constructing a coaxial multiphase flame jet that could be adapted in continuous-flow manufacture. Although a rotating system has been introduced for continuous manufacture of carbon nanoparticles from hydrocarbon flames,[28,29] there are no reports of FAS for the continuous production of G-containing composites. The prototype consisted of coaxial channels for three different flows to produce multiphase coaxial reactions of MoS_2 dots (or CdS, directly supplied after the photoinduced sulfidation of ultrafine Mo (or Cd) particles,[30,31] inner channel), titanium isopropoxide vapors (TTIP, titanium (Ti) feedstock,[32,33] middle channel), and an ethanol solution (carbon feedstock and heat,[34,35] outer channel) (**Figure 1**). Circularly conveying nickel–copper (Cu–Ni) alloy foil within the flame induced aerosol self-assembly[36] between the MoS_2 (or CdS, particle-laden ambient nitrogen (N_2) gas flow)–TiO_2 (TTIP pyrolysis and subsequent Ti oxidation) hybrids and the catalytically grown G nanosheets from hydrocarbons on the moving foil (carbon dissolution and precipitation on Cu–Ni) to form MoS_2–TiO_2@G (or CdS–TiO_2@G) ternary composites. The collected composites from ultrasonication (for detachment of the composites from the foil and subsequent homogenization of the dispersed composites) and subsequent spray drying (for in-line size observation and collection on substrates for physicochemical characterizations and photocatalytic applications) were transferred to reactors to determine their photocatalytic performance in H_2 production and CO_2 reduction.

2. Results and Discussion

A scanning mobility particle sizer (SMPS) system was used for the in-line inspection of the resulting materials because the size distribution measurement can be performed in-flight by direct sampling of the resulting mechanically sprayed materials after passing through the diffusion dryer (Figure S1A, Supporting Information). As shown in Figure S1B, Supporting Information, the size distribution profiles of the individual MoS_2 and TiO_2 particles clearly show differences in the geometric mean diameter (21.7 nm for MoS_2 and 53.9 nm for TiO_2), which match the difference in the supply configuration (direct particle supply for MoS_2 versus TTIP vapor supply for pyrolysis-made TiO_2). Interestingly, no peaks for MoS_2 were observed after incorporation between the MoS_2 and TiO_2 particles (MoS_2–TiO_2), while

the profile of MoS_2–TiO_2 was analogous to that of individual TiO_2. This represents the quantitative incorporation of MoS_2 onto pyrolysis-made TiO_2 particles in the reaction zone where thermophoresis between the different environmental temperatures of MoS_2 and TiO_2 particle flows that derived a similarity in the geometric standard deviation (GSD) between TiO_2 and MoS_2–TiO_2 particles (Table S1, Supporting Information). On the other hand, the GSD of G exhibited a higher value than those of TiO_2 and MoS_2–TiO_2, which may be caused by the ultrasonic detachment and subsequent redistribution of catalytically grown G layers on the Cu–Ni foil. Nevertheless, the incorporation of MoS_2–TiO_2 and G in the course of the ultrasonic process could allow the reconstruction of the resulting materials with unimodal size distribution. This eventually reduced the GSD (2.30 to 1.94) of G, which supports the tight conjugation between MoS_2–TiO_2 and G. As another in-line inspection of the resulting materials, Raman spectroscopy was used to validate composite formation because it is workable for the rapid observation of a compositional and strain metrology throughout single-pass material processing.[37,38] The resulting materials after mechanical spraying and subsequent diffusion drying were deposited directly on a glass disc and placed in a Raman spectrometer (Figure S2A, Supporting Information). The bands around 150 cm^{-1} ($E_{g(1)}$), 400 cm^{-1} ($B_{1g(1)}$), 520 cm^{-1} ($A_{1g} + B_{1g(2)}$), and 640 cm^{-1} ($E_{g(2)}$) were observed for TiO_2, confirming the formation of anatase,[12] while the shoulder peaks at around 380 cm^{-1} ($E_{1g(2)}$) and 410 cm^{-1} (A_{2g}) in MoS_2–TiO_2 matched the in-plane and out of plane vibrations of the S atom, supporting the presence of MoS_2.[39] The peaks at ≈1350 cm^{-1} (D-band) and 1590 cm^{-1} (G-band) represented the graphitized structures (matched the characteristic bands of reduced graphene oxide),[12] confirming the catalytic growth of G layers on the rotating Cu–Ni foil. The hydrocarbons from decomposition of the injected ethanol and methane may be dissolved and saturated in the Cu–Ni foil catalyst, and successively, the carbon solubility in the catalyst decreased sharply as the foil leaves the flame, resulting in carbon precipitation to form G layers.[27] The slightly higher intensity of the D-band (disordered graphite) than that of the G-band (crystalline graphite) suggested a higher degree of defects in the G layers, probably due to wrinkling and folding during the ultrasonic detachment and dispersion of the G layers on the Cu–Ni foil.[40] These structural defects may also be related to the quenching by rotation of the foil in which moving catalyst may cause carbon scarcity on the catalyst surface, particularly in the region of low temperature.[41] MoS_2–TiO_2@G configuration included the characteristic bands of the individual components, which provides evidence for constructing ternary composites. According to the aerosol size distributions and Raman spectra, SMPS and Raman spectroscopy were workable for in-line validation of ternary composites assembled through the single-pass FAS and subsequent ultrasonic detachment and dispersion. To prove further the formation of MoS_2–TiO_2@G configuration, the collected samples were placed in an X-ray diffractometer to identify coexistence of MoS_2, TiO_2, and G components. Figure S2B, Supporting Information exhibits characteristic bands for anatase TiO_2 (25.3°, 37.9°, 48.2°, 54.1°, and 62.7°), hexagonal MoS_2 (14.2°, 32.6°, and 58.3°), and G (≈23°),[42] demonstrating the incorporation of the three components during the continuous manufacture.

As shown in **Figure 2**A, the morphology and microstructure of the resulting materials were observed by transmission electron microscopy (TEM) after the spray-dried materials had been collected directly on the carbon-coated copper grids. A representative TEM image of MoS_2 confirmed the fine dots (2.9 nm of average diameter), and the high-magnification image for the individual dots mainly exhibited an interplanar distance (*d*) of 0.27 nm, corresponding to the (100) plane of hexagonal lattice-structured MoS_2 quantum dots.[43] On the other hand, the suprastructures of TiO_2 particles with a *d*-spacing of 0.35 nm ((101) crystal plane of anatase TiO_2)[44] were observed, probably due to the agglomeration of primary particles during TTIP pyrolysis and subsequent oxidation at high temperatures. For the MoS_2–TiO_2 configuration, thermophoresis from the temperature difference between the MoS_2- and TiO_2-laden flow induced the intervention of MoS_2 dots in a TiO_2 supraparticle (coexistence of different *d*-spacing values ($d_{100, MoS2}$ and $d_{101, TiO2}$) in the high-magnification image), which induces a distortion of the TiO_2 supraparticles. This suggests that the coaxial flow reaction is workable to generate intimate interfacial contacts between MoS_2 and TiO_2 spontaneously to facilitate the separation and transfer of photogenerated charge carriers within the interfaces. In the case of G, folded edges similar to the flame produced G nanosheets in a previous report[45] were observed even after G layers were detached from Cu–Ni foil, and the high-magnification image revealed G lattice fringes (0.36 nm of interlayer spacing),[44] which matched G nanosheets detached under ultrasonication in a previous report.[46] TEM of the resulting materials from all-flows-inclusive flame reaction revealed the decoration of distorted MoS_2–TiO_2 supraparticles in which two different interplanar distances were anchored on the graphitic fringes, proving the generation of MoS_2–TiO_2@G ternary interfaces. Furthermore, the observed hexagonal MoS_2 and anatase TiO_2 microstructures, including graphitic fringes of G are consistent with characteristic bands in the Raman spectra, supporting the validity of Raman spectroscopy for prompt verification of the resulting materials from a single-pass assembly. A representative atomic force microscopy (AFM) image obtained after direct deposition of the resulting MoS_2–TiO_2@G on an ultra-flat silicon wafer revealed several dimples (200–300 nm in lateral dimension), which may be due to MoS_2–TiO_2 packing on G likely through capillary suction of voids in the folded G nanosheets.[47] The particles collected on the silicon wafer were observed by scanning electron microscopy (SEM) to confirm the outward form of MoS_2–TiO_2@G, as shown in Figure 2B. The image exhibited that a thin crumpled layer holds a bunch of particles, observing a dimpled surface on the wafer at the AFM. The corresponding energy-dispersive X-ray (EDX) maps exhibited dot distributions of elemental Mo, Ti, and C coinciding with the particle, validating further the assembly of the ternary composites from the flame reaction and subsequent ultrasonic process in a continuous manner.

The surface states of the resulting MoS_2–TiO_2@G were determined by X-ray photoelectron (XPS). The Mo $3d$ core-level XPS spectra of the MoS_2 (Figure S3, Supporting Information) at 228.3 and 232.2 eV matched the Mo^{IV} $3d_{5/2}$ and Mo^{IV} $3d_{3/2}$, respectively, while the other peaks at ≈225 and 235 eV belong to S 2s and Mo^{VI}, respectively. The S 2p core-level spectra exhibited peaks at 162.2 (S $2p_{3/2}$) and 163.1 (S $2p_{1/2}$) eV, including
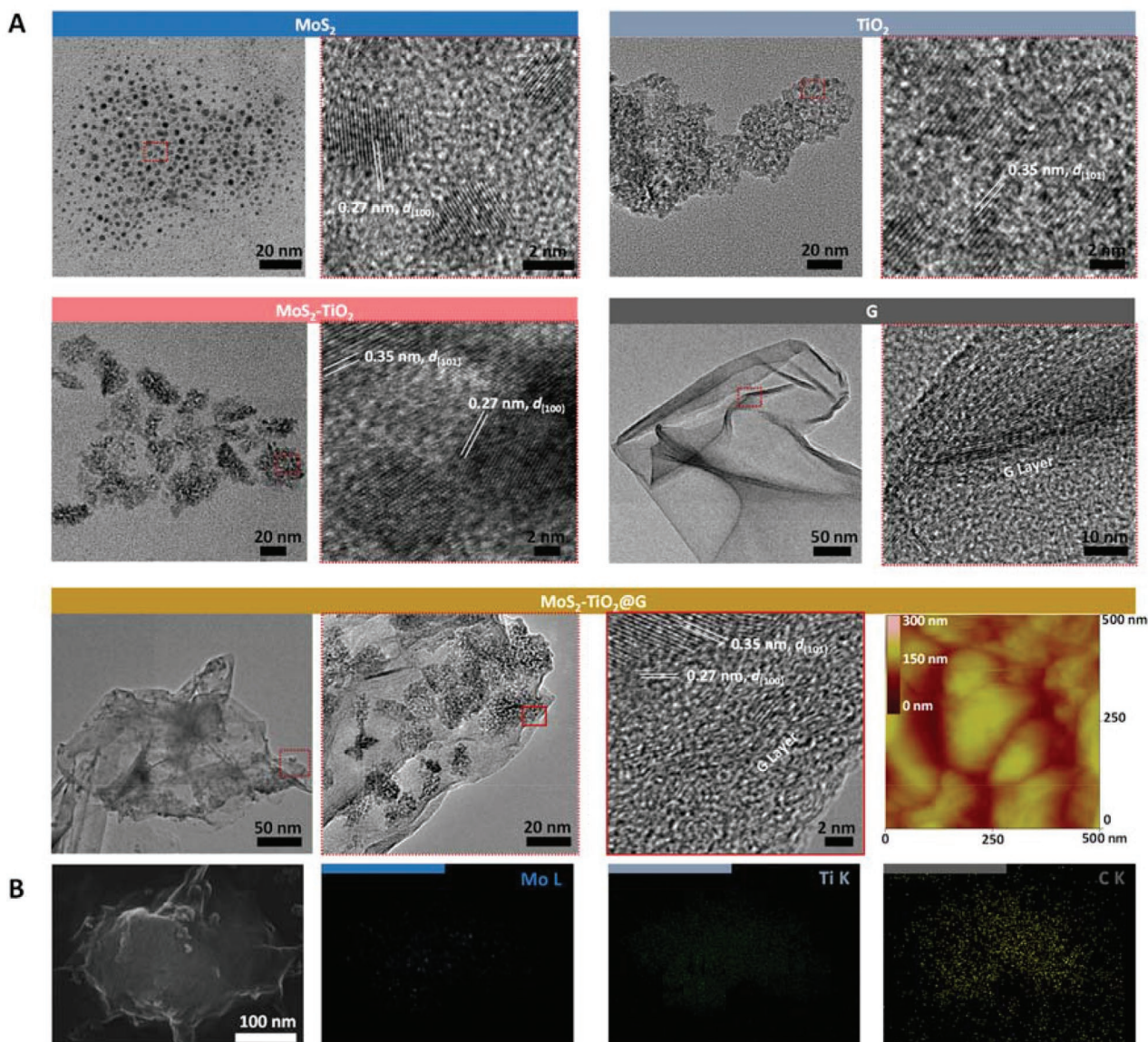
Figure 2. Morphological and compositional analyses of the resulting MoS$_2$–TiO$_2$@G, as well as individual components for comparison. A) Low- and high-magnification TEM image of MoS$_2$, TiO$_2$, MoS$_2$–TiO$_2$, and G. The high-magnification images correspond to the dotted (or solid) boxes in the low-magnification images. The spray-dried particles were deposited directly on carbon-coated copper grids using a mechanical aerosol sampler. Images for MoS$_2$–TiO$_2$@G include a representative AFM profile after the composites were collected on a silicon wafer substrate. B) A representative SEM image of a MoS$_2$–TiO$_2$@G on a silicon wafer substrate and its elemental maps to examine the distribution of the major elements (Mo, Ti, and C).

168.1 (S^{VI}) eV, indicating the existence of MoS$_2$ dots (i.e., the formation of Mo–S bindings) in the ternary composite. A comparison with the core-level Mo and S spectra for MoS$_2$ dots in previous reports[48–50] revealed differences in the peak intensity and binding energy. These might be due to thermophoretic MoS$_2$ intervening in TiO$_2$ at high temperatures that lead to strong interfacial contact between the directly supplied MoS$_2$ and pyrolysis generated TiO$_2$ and the slight oxidation of the supplied MoS$_2$ dots during the MoS$_2$–TiO$_2$ supraparticle formation. The binding energies of Ti 2p in the composite were observed at 458.6 (Ti 2p$_{3/2}$) and 464.4 (Ti 2p$_{1/2}$) eV, confirming that TTIP pyrolysis in the flame can generate normal surface states of Ti^{IV} in TiO$_2$.[51] The O 1s core spectra showed the formation of Ti–O

bindings in TiO$_2$ and clarified the contacts between TiO$_2$ and G (C–O and O–H in carbon) formed during the flame reaction. The C 1s profile showed three peaks at 284.8, 286.4, and 288.7 eV, which were assigned to C–C, C–O, and O=C–O functionalities, respectively,[52,53] supporting the formation of G layers and the existence of Ti–O–C and Ti–O–H peaks in the O 1s profile. The characteristic peaks and shift in the binding energies in the obtained core level spectra represented further construction of the ternary composites, supporting the generation of strong interfacial contacts among the MoS$_2$, TiO$_2$, and G from the coaxial multiphase flame. In addition, the mass fractions of MoS$_2$, TiO$_2$, and G in the composite were estimated to 0.06, 0.82, and 0.12, respectively, which are comparable
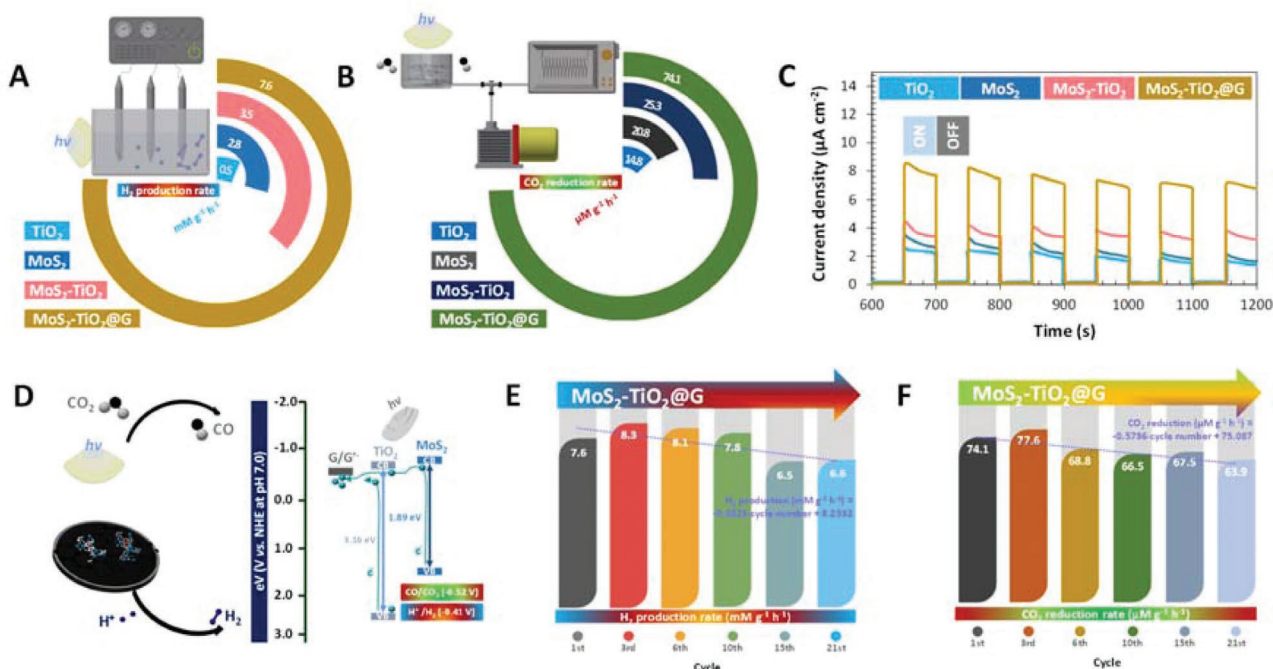
Figure 3. Photoinduced H_2 production, CO_2 reduction, transient photocurrent profiles of MoS_2–TiO_2@G with an illustration of the photogenerated electron path in the composite. A,B) Comparison of the resulting MoS_2–TiO_2@G and TiO_2 (or MoS_2, MoS_2–TiO_2) for H_2 production and CO_2 reduction. The schematics for the production and reduction are depicted as insets. C) Transient photocurrent responses of the resulting MoS_2–TiO_2@G (in 0.5 M Na_2SO_4 solution at 0.5 V versus Ag/AgCl), including TiO_2, MoS_2, and MoS_2–TiO_2 in the presence and absence of visible light irradiation (>420 nm of wavelength). D) Electronic band diagrams for the components of the MoS_2–TiO_2@G in the presence of visible light irradiation to support H_2 production and CO_2 conversion due to photogenerated electron transfer. E,F) Stabilities of the MoS_2–TiO_2@G for H_2 production and CO_2 reduction during 21 reaction cycles. The equations of trend lines for the production and reduction are provided.

with those obtained using EDX analyses (Figure 2B) and the analogous composites in previous reports.[12,13]

The effectiveness of the continuous-flow manufacture was identified by testing H_2 production and CO_2 reduction, including the transient current density of the resulting MoS_2–TiO_2@G under visible light irradiation. MoS_2 dots exhibited significantly lower rates in H_2 production (**Figure 3**A) and CO_2 reduction (Figure 3B) than those of MoS_2–TiO_2 and MoS_2–TiO_2@G, probably because of the short lifetime of the photogenerated charge carriers (fast recombination of conduction band (CB) electrons and valence band (VB) holes). The contacts between MoS_2 and TiO_2 through the intervening MoS_2 dots in the TiO_2 suprastructure may impede the electron-hole recombination that enhances the rates of H_2 production and CO_2 reduction. The incorporation between the MoS_2–TiO_2 supraparticles and G nanosheets further enhanced the H_2 production (reaching 7.6 mM $g^{-1}h^{-1}$) and CO_2 reduction (reaching 74.1 μM $g^{-1}h^{-1}$) rates where contacts between TiO_2 and G facilitated the transfer and distribution of electrons to the surfaces of G, impeding further charge recombination. This phenomenon induced differences in the charge transport pathway between the configurations (MoS_2, MoS_2–TiO_2, and MoS_2–TiO_2@G), as shown in Figure 3C, and the rates matched the transient current density under visible light irradiation. Hence, a higher concentration of photogenerated electrons between MoS_2–TiO_2 and G compared to those in TiO_2 (or MoS_2, MoS_2–TiO_2) could generate greater yields in H_2 and CO formation by reducing the adjacent H^+ and CO_2. In addition, differences in light

absorption between the configurations (Figure S4, Supporting Information; matched the increased light absorption in the visible range (>400 nm wavelength) upon incorporation between MoS_2–TiO_2 and G (forming Ti−O−C bonds))[39,54,55] further affected the amount of reactive electrons to be reacted with H^+ and CO_2 in the ternary composite. Figure 3D shows the possible transport pathways of photogenerated electrons on the electronic band diagrams for demonstrating the photocatalytic reductions. Under visible light irradiation, MoS_2 and TiO_2 on the G nanosheets may be excited simultaneously to induce an electron transition from the VB to the CB. Because of the more negative CB potential of MoS_2 than TiO_2, the excited electrons on the CB of MoS_2 tended to transfer to CB of TiO_2, which induce electron accumulation on the CB of TiO_2. Owing to the excellent electrical conductivity of G nanosheets, the accumulated electrons were transported rapidly and distributed over the surface of nanosheets with no significant recombination of electron and hole pairs. The electrons on the nanosheets eventually led to the reduction of adsorbed H^+ and CO_2 on the nanosheets, which supported the significantly higher reduction rates of MoS_2–TiO_2@G than TiO_2 (or MoS_2, MoS_2–TiO_2). The binding energies (E_b) between the interfaces were determined using SIESTA code based on the characterized results as well as previous relevant studies.[56,57] The resulting E_b values were −0.1, −1.2, −3.5, and −2.8 eV for MoS_2–TiO_2, MoS_2@G, TiO_2@G, and MoS_2–TiO_2@G interfaces, respectively. The greater E_b of TiO_2@G (more negative E_b values correspond to stronger interfacial bindings) than those of MoS_2–TiO_2

and $MoS_2@G$ may generate the electron pathway from MoS_2 to G through TiO_2, which is in agreement with the hypothetical pathway for H_2 production and CO_2 reduction on G nanosheets. The greater E_b of $TiO_2@G$ even than MoS_2–$TiO_2@G$ (MoS_2 dots affected the bindings between TiO_2 and G) also supports the electron accumulation over the surface of G nanosheets that leads to the enhanced photocatalytic reactions. Incorporating MoS_2 (0.06) and G (0.12) as accessory ingredients[12] with low cost TiO_2 (0.82)[58] to generate electron pathway from MoS_2 to G as well as electron accumulation over the G surfaces enhanced significantly the photocatalytic activities. The stabilities of MoS_2–$TiO_2@G$ in both H_2 production and CO_2 reduction were determined by measuring the reaction rates for 21 cycle tests. As shown in Figure 3E,F, the resulting rates for both H_2 production and CO_2 reduction were more than 86% of their initial value after 21 cycles. These might be related to natural thermal curing at the high flame temperatures during the assembly of MoS_2–$TiO_2@G$, which induces higher solidities in the composite structure and interfacial contact between the components. This result further supports the suitability of utilizing a coaxial multiphase flame to assemble ternary nanocomposites with superior and stable photocatalytic activities.

Modulation of the ternary composite construction was achieved by supplying CdS dot-laden N_2 flow from the photoinduced sulfidation of ultrafine aerosol Cd particles[59] instead of the MoS_2 for the coaxial multiphase flame. Representative low- and high-magnification TEM images of the supplied CdS dots into the inner channel exhibited singlet particles (3.2 nm of average diameter) with a d of 0.20 nm corresponding to the (220) crystalline plane for CdS quantum dots (Figure S5A, Supporting Information).[11] The representative TEM images of CdS–TiO_2 and CdS–$TiO_2@G$ exhibited analogous architectures to MoS_2–TiO_2 and MoS_2–$TiO_2@G$ with no disturbances to the formation of anatase TiO_2 supraparticles and wrinkled G nanosheets (high-magnification TEM images). This suggests that the thermophoretic attraction between the CdS and TiO_2 is also workable for the intervening CdS dots in TiO_2 supraparticles to form CdS–TiO_2 and CdS–$TiO_2@G$ architectures. From EDX analyses, the mass fractions of CdS, TiO_2, and G in the composite were 0.07, 0.81, and 0.12, respectively, which are similar to those of MoS_2–$TiO_2@G$, suggesting the modular ability of the coaxial multiphase flame for achieving different composite structures with almost identical composition ratios between the constituents. Figure S5B, Supporting Information presents the comparative profiles of transient current density between the CdS–$TiO_2@G$ and CdS (or CdS–TiO_2) during on–off repetitions of visible light irradiation. The significantly higher current levels of CdS–$TiO_2@G$ may be due to the suppressed charge recombination where photogenerated electrons in the CB of CdS are transferred to TiO_2 and G through the interfaces by providing prolonged charge transport[60,61] for the promoted surface chemical reactions to reduce the adjacent H^+ and CO_2 compared to CdS and CdS–TiO_2, as shown in Figure S5C,D, Supporting Information. The resulting initial rates of H_2 production and CO_2 reduction reached 8.1 mm g^{-1} h^{-1} and 79.9 μm $g^{-1}h^{-1}$, respectively; the rates were greater than 94% of their initial value after 21 cycles, due likely to solidity in the composite structure and interfacial contacts in accordance with MoS_2–$TiO_2@G$. The slightly greater rates than those

of MoS_2–$TiO_2@G$ could be attributed to the higher transient current density because the textural properties of the two ternary composites obtained using a porosimeter exhibited nearly identical adsorption–desorption isotherms (type IV) and pore size distributions (mesoporous structure related to voids at the interfacial contacts between the components)[62] (Figure S6, Supporting Information) as well as surface areas and pore volumes (Table S2, Supporting Information). This shows that the coaxial multiphase flame is further workable to construct comparable textural properties, even for different compositions, enabling parametric control of the photocatalytic activity by reconfiguring the quantum dot-laden flow.

The reconfigurable ability of the coaxial flame was validated further to construct the different nanocomposites through replacement of Mo (or TTIP) with Pb (or zinc acetate). PbS aerosol (photoinduced sulfidation of spark ablated Pb particles) was incorporated with TiO_2 and subsequently deposited over G nanosheets to form PbS–$TiO_2@G$. In the case of MoS_2–$ZnO@G$ manufacture, zinc acetate vapor-laden CH_4–air was injected into the middle slit of the coaxial burner to supply ZnO for incorporation with MoS_2 to form MoS_2–ZnO. Representative low- and high-magnification TEM images (Figure S7, Supporting Information) revealed similar constructs and interfaces with MoS_2–$TiO_2@G$ and CdS–$TiO_2@G$ even replacing TTIP by zinc acetate to generate ZnO particles instead of TiO_2, warranting modular property of the coaxial flame to a variety of photocatalytic nanocomposites for H_2 production and CO_2 reduction.

In addition, the validity of processing cost was assessed by comparing the estimated necessary expenses (chemicals, fuel, equipment, and others to manufacture 1 kg)[63] for between TiO_2 alone and MoS_2–$TiO_2@G$ using the lab-scale coaxial burner. The total costs for TiO_2 alone and MoS_2–$TiO_2@G$ were 177.4 and 745.1 USD, respectively. Additional costs generated from electricity and other chemicals and equipment caused about four times increase of cost for the composite manufacture. On the other hand, the costs to manufacture 1 kg of TiO_2 particles using sol–gel and chemical precipitation processes in previous studies[64,65] reached 356.6 and 184.1 USD, respectively. Furthermore, the rates of H_2 production (7.6 mm $g^{-1}h^{-1}$) and CO_2 reduction (74.1 μm $g^{-1}h^{-1}$) achieved from MoS_2–$TiO_2@G$ were significantly greater that those from TiO_2 alone (0.5 mm $g^{-1}h^{-1}$ and 14.8 μm $g^{-1}h^{-1}$). This suggests that the developed manufacture could have an actual competitive advantage in the applications despite the need for constructing the coaxial multiphase flame and its ancillary devices.

3. Conclusion

A coaxial multiphase flame was established for the low-cost, continuous, and modulatable production of ternary G composites that combined a rotating Cu–Ni foil and ultrasonic bath for the catalytic growth of G and the collection of the composites after the incorporation of MoS_2 and TiO_2 particles with the G grown in a single-pass configuration. Each flow provided the continual supply of MoS_2 aerosol-laden N_2 (inner flow), TTIP vapor-laden CH_4-air (middle flow), and liquid ethanol (outer flow) into the flame for the catalytic growth of G (based on

Einstein diffusion equation for setting the location of Cu–Ni foil) and the subsequent deposition of MoS_2–TiO_2 particles on a rotating Cu–Ni foil with a production rate of >10 g h^{-1} per single flame. Replacing the inner flow with the CdS aerosol produced CdS–TiO_2@G, which had the potential for the reconfigurable production of G-containing composites by adjusting the composition of each flow. The collected composites from ultrasonication were used as active materials for photocatalytic energy conversion processes. The yields and stabilities of the resulting composites for H_2 production (>6.5 mm g^{-1}h^{-1}) and CO_2 reduction (>60 μm g^{-1}h^{-1}) were comparable to those from analogous ternary composites introduced in recent reports. The coaxial multiphase flame and the resulting materials may offer a simple, scalable, and realizable strategy for assembling composite photocatalysts and providing an implementable platform for reconfigurable G-included composite manufacture for various energy and environmental applications.

4. Experimental Section

A custom circular coaxial burner (44 mm, outer diameter) consisting of three circular slits was used to generate a multicomponent flame, where MoS_2 aerosol (photoinduced sulfidation of spark ablated Mo particles)[55]-laden N_2 (1.5 L min^{-1}), TTIP (0.8 m) vapor-laden CH_4 (1.5 L min^{-1})-air (3.0 L min^{-1}), and liquid ethanol (4.5 mL min^{-1}) flows, respectively, passed the inner, middle, and outer slits to generate a flame (≈860°C, average temperature). The Cu–Ni alloy foil (0.5 mm thickness, 5.0 cm width) circularly passed (52 s duration) upside (at a distance of 3 cm) between the slits for TTIP vapor-laden CH_4–air, and liquid ethanol flows (Figure 1), in which the gap distance between the ethanol slit and Cu–Ni foil was aligned by correspondingly considering the Einstein diffusion equation ($d_t = \sqrt{2Dt_d}$, where d_t, D, and t_d are the travel distance, diffusion coefficient, and required diffusion time for hydrocarbons onto the foil, respectively) and the resulting composite structures. The pyrolysis and subsequent segregation of hydrocarbons (from ethanol and methane) on surfaces of the rotating foil induced the catalytic growth of graphene layers,[66] while TiO_2 (from TTIP pyrolysis and subsequent Ti oxidation)[67] and MoS_2 particles agglomerated thermophoretically (forming MoS_2–TiO_2) because of the significant differences in gas temperature between the flows. The thermal behaviors of the formed MoS_2–TiO_2 particles induced their random deposition on the grown graphenes, resulting in the formation of MoS_2–TiO_2@G ternary composites. The composites on the foil were then immersed by rotation in an ultrasonic probe (20 kHz) immersed bath (25 w/v% $FeCl_3$ in ethanol) to harvest the composites from the foil. The composite dispersed solution was spray-dried using a serially connected mechanical spray and diffusion dryer to extract the solvent from the composites. The composites were finally collected on a membrane filter (11807-47-N, Sartorius, Germany), rinsed with ethanol, and dried with N_2 for use as an active material for H_2 production and CO_2 reduction in the presence of visible light irradiation.

The resulting ternary composites (MoS_2–TiO_2@G and CdS–TiO_2@G) were transferred for photocatalytic H_2 production and CO_2 reduction in a closed circulation reactor. In the case of H_2 production, the vacuum-dispersed (removing dissolved oxygen) composites (0.25 mg composite mL^{-1}·0.5 m Na_2SO_4) were exposed to a 300 W xenon lamp containing a 420 nm cut-off filter (LOT-Oriel, Germany) with an irradiation intensity of 0.18 W cm^{-2}. The concentration of the H_2 produced under magnetic agitation was monitored using a gas chromatography (GC) with a thermal conductivity detector (6890, Agilent, USA). The CO_2 reduction rate was determined by depositing the composites on a circular stainless steel plate by spreading the dried powder of the composites, followed by dripping deionized water to form a plaster. The plate was then placed in a cylindrical quartz reactor, and the reactor was purged with CO_2 for 1 h at 45 °C and sealed before light

irradiation (300 W xenon lamp for 4 h). The CO_2 concentration was also detected using GC for estimating the reduction rates.

Conflict of Interest

The authors declare no conflict of interest.

Data Availability Statement

The data that support the findings of this study are available in the supplementary material of this article.

[1] Z. Sun, N. Talreja, H. Tao, J. Texter, M. Muhler, J. Strunk, J. Chen, *Angew. Chem., Int. Ed.* **2018**, *57*, 7610.

[2] M. Faraji, M. Yousefi, S. Yousefzadeh, M. Zirak, N. Naseri, T. H. Jeon, W. Choi, A. Z. Moshfegh, *Energy Environ. Sci.* **2019**, *12*, 59.

[3] J. K. Stolarczyk, S. Bhattacharyya, L. Polavarapu, J. Feldmann, *ACS Catal.* **2018**, *8*, 3602.

[4] Q. Xiang, B. Cheng, J. Yu, *Angew. Chem., Int. Ed.* **2015**, *54*, 11350.

[5] M. Majdoub, Z. Anfar, A. Amedlous, *ACS Nano* **2020**, *14*, 12390.

[6] E. Rani, P. Talebi, W. Cao, M. Huttula, H. Singh, *Nanoscale* **2020**, *12*, 23461.

[7] X. Sun, L. Shi, H. Huang, X. Song, T. Ma, *Chem. Commun.* **2020**, *56*, 11000.

[8] X. Zeng, X. Xiao, W. Zhang, C. Wan, H. Wang, *Comput. Mater. Sci.* **2017**, *126*, 43.

[9] A. Hasani, M. Tekalgne, Q. V. Le, H. W. Jang, S. Y. Kim, *J. Mater. Chem. A* **2019**, *7*, 430.

[10] W. Gao, M. Wang, C. Ran, L. Li, *Chem. Commun.* **2015**, *51*, 1709.

[11] Y. Lu, X. Cheng, G. Tian, H. Zhao, L. He, J. Hu, S.-M. Wu, Y. Dong, G.-G. Chang, S. Lenaerts, S. Siffert, G. V. Tendeloo, Z.-F. Li, L.-L. Xu, X.-Y. Yang, B.-L. Su, *Nano Energy* **2018**, *47*, 8.

[12] Q. Xiang, J. Yu, M. Jaroniec, *J. Am. Chem. Soc.* **2012**, *134*, 6575.

[13] H. Jung, K. M. Cho, K. H. Kim, H.-W. Yoo, A. Al-Saggaf, I. Gereige, H.-T. Jung, *ACS Sustainable Chem. Eng.* **2018**, *6*, 5718.

[14] S. Kang, H. Khan, C. S. Lee, *Sol. Energy Mater. Sol. Cells* **2021**, *221*, 110890.

[15] D. Deng, K. S. Novoselov, Q. Fu, N. Zheng, Z. Tian, X. Bao, *Nat. Nanotechnol.* **2016**, *11*, 218.

[16] N. R. Chodankar, A. K. Nanjundan, D. Losic, D. P. Dubal, J.-B. Baek, *Mater. Today Adv.* **2020**, *6*, 100053.

[17] K. Khan, A. K. Tareen, M. Aslam, Y. Zhang, R. Wang, Z. Ouyang, Z. Gou, H. Zhang, *Nanoscale* **2019**, *11*, 21622.

[18] L. Yang, W. Chen, Q. Yu, B. Liu, *Nano Res.* **2021**, *14*, 1583.

[19] G. H. Jeong, S. P. Sasikala, T. Yun, G. Y. Lee, W. J. Lee, S. O. Kim, *Adv. Mater.* **2020**, *32*, 1907006.

[20] D. Qin, Y. Zhou, W. Wang, C. Zhang, G. Zeng, D. Huang, L. Wang, H. Wang, Y. Yang, L. Lei, S. Chen, D. He, *J. Mater. Chem. A* **2020**, *8*, 19156.

[21] Y. Sheng, M. Kraft, R. Xu, *Curr. Opin. Chem. Eng.* **2018**, *20*, 39.

[22] W. J. Sharmach, R. D. Buchner, V. Papavassiliou, P. Pacouloute, M. T. Swihart, *Aerosol Sci. Technol.* **2010**, *44*, 1083.

[23] G. A. Kelesidis, S. E. Pratsinis, *Chem. Eng. J.* **2021**, *421*, 129884.

[24] M. M. Mohammadi, S. S. Gunturi, S. Shao, S. Konda, R. D. Buchner, M. T. Swihart, *Chem. Eng. J.* **2019**, *372*, 648.

[25] B. Aissa, N. K. Memon, A. Ali, M. K. Khraisheh, *Front. Mater.* **2015**, *2*, 58.

[26] N. K. Memon, B. H. Kear, S. D. Tse, *Chem. Phys. Lett.* **2013**, *570*, 90.

[27] M. Qian, C. Xu, Y. Gao, *Mater. Sci. Eng. B* **2018**, *238*, 149.

[28] C. Yang, Z. Li, Y. Huang, K. Wang, Y. Long, Z. Guo, X. Li, H. Wu, *Nano Lett.* **2021**, *21*, 3198.

[29] S. Dong, Z. Wang, Y. Wang, X. Bai, Y. Q. Fu, B. Guo, C. Tan, J. Zhang, P. Hu, *ACS Appl. Mater. Interfaces* **2018**, *10*, 2174.

[30] J. H. Byeon, J. T. Roberts, *Chem. Mater.* **2012**, *24*, 3544.

[31] B. K. Poudel, J. O. Kim, J. H. Byeon, *Adv. Sci.* **2018**, *5*, 1700563.

[32] L. G. Bettini, M. V. Dozzi, F. D. Foglia, G. L. Chiarello, E. Selli, C. Lenardi, P. Piseri, P. Milani, *Appl. Catal. B* **2015**, *178*, 226.

[33] K. B. Riad, P. M. Wood-Adams, K. Wegner, *Mater. Res. Bull.* **2018**, *106*, 276.

[34] X. Du, H.-Y. Liu, Y.-W. Mai, *ACS Nano* **2016**, *10*, 453.

[35] Z. Li, H. Zhu, K. Wang, J. Wei, X. Gui, X. Li, C. Li, L. Fan, P. Sun, D. Wu, *Carbon* **2011**, *49*, 237.

[36] J. Ryu, S. Kim, H. I. Kim, E.-H. Jo, Y. K. Kim, M. Kim, H. D. Jang, *Chem. Eng. J.* **2015**, *262*, 409.

[37] F. Yang, X. Wang, D. Zhang, J. Yang, D. Luo, Z. Xu, J. Wei, J.-Q. Wang, Z. Xu, F. Peng, X. Li, R. Li, Y. Li, M. Li, X. Bai, F. Ding, Y. Li, *Nature* **2014**, *510*, 522.

[38] D. Schmidt, C. Durfee, J. Li, N. Loubert, A. Cepler, L. Neeman, N. Meir, J. Ofek, Y. Oren, D. Fishman, in *Proc. SPIE*, Vol. *11611*, International Society for Optics and Photonics, Bellingham **2021**, p. 116111T.

[39] D. B. Nimbalkar, H.-H. Lo, P. V. R. K. Ramacharyulu, S.-C. Ke, *RSC Adv.* **2016**, *6*, 31661.

[40] F. Carraro, M. Cattelan, M. Favaro, L. Calvillo, *Nanomaterials* **2018**, *8*, 406.

[41] Y. Zhang, B. Cao, B. Zhang, X. Qi, C. Pan, *Thin Solid Films* **2012**, *520*, 6850.

[42] Z. Chen, Y. Liu, W. Zhang, X. Guo, Y. Zheng, X. Tang, Y. Wang, Y. Zhang, Z. Wang, T. Zhang, *J. Mater. Sci.: Mater. Electron.* **2019**, *30*, 12901.

[43] M. Kukkar, S. Singh, N. Kumar, S. K. Tuteja, K.-H. Kim, A. Deep, *Microchim. Acta* **2017**, *184*, 4647.

[44] Q. Quan, S. Xie, B. Weng, Y. Wang, Y.-J. Xu, *Small* **2018**, *14*, 1704531.

[45] M. M. Mohammadi, S. Shao, S. S. Gunturi, A. R. Raghavan, N. Alexander, Y. Liu, C. M. Stafford, R. D. Buchner, M. T. Swihart, *Nanoscale* **2019**, *11*, 19571.

[46] T. Lin, Y. Wang, H. Bi, D. Wan, F. Huang, X. Xie, M. Jiang, *J. Mater. Chem.* **2012**, *22*, 2859.

[47] J. H. Byeon, Y.-W. Kim, *RSC Adv.* **2013**, *3*, 7259.

[48] W. Gu, Y. Yan, C. Zhang, C. Ding, Y. Xian, *ACS Appl. Mater. Interfaces* **2016**, *9*, 11272.

[49] X. Zhu, J. Xiang, J. Li, C. Feng, P. Liu, B. Xiang, *J. Colloid Interface Sci.* **2018**, *511*, 209.

[50] B. Chen, E. Liu, T. Cao, F. He, C. Shi, C. He, L. Ma, Q. Li, J. Li, N. Zhao, *Nano Energy* **2017**, *33*, 247.

[51] B. Chen, N. Zhao, C. Wei, J. Zhou, F. He, C. Shi, C. He, E. Liu, *Appl. Surf. Sci.* **2017**, *401*, 232.

[52] Y. Gao, Y. Zheng, J. Chai, J. Tian, T. Jing, D. Zhang, J. Cheng, H. Peng, B. Liu, G. Zheng, *RSC Adv.* **2019**, *9*, 15033.

[53] J. Ma, M. Xing, L. Yin, K. S. Hui, K. N. Hui, *Appl. Surf. Sci.* **2021**, *536*, 147735.

[54] W. Han, C. Zang, Z. Huang, H. Zhang, L. Ren, X. Qi, J. Zhong, *Int. J. Hydrogen Energy* **2014**, *39*, 19502.

[55] H. Qiao, Z. Huang, S. Liu, Y. Tao, H. Zhou, M. Li, Z. Qi, *J. Phys. Chem. C* **2019**, *123*, 10949.

[56] M. Dion, H. Rydberg, E. Schröder, D. C. Langreth, B. I. Lundqvist, *Phys. Rev. Lett.* **2004**, *92*, 246401.

[57] A. B. Alencar, A. P. M. Barboza, B. S. Archanjo, H. Chacham, B. R. A. Neves, *2D Mater.* **2015**, *2*, 015004.

[58] A. J. Gröhn, S. E. Pratsinis, A. Sánchez-Ferrer, R. Mezzenga, K. Wegner, *Ind. Eng. Chem. Res.* **2014**, *53*, 10734.

[59] B. K. Poudel, K.-O. Doh, J. H. Byeon, *Green Chem.* **2018**, *20*, 978.

[60] S. Dutta, R. Sahoo, C. Ray, S. Sarkar, J. Jana, Y. Negishi, T. Pal, *Dalton Trans.* **2015**, *44*, 193.

[61] Y. Zhang, C. Wang, Z. Yuan, L. Zhang, L. Yin, *Eur. J. Inorg. Chem.* **2017**, *2017*, 2281.

[62] W. Zhang, X. Xiao, Y. Li, X. Zeng, L. Zheng, C. Wan, *Appl. Surf. Sci.* **2016**, *389*, 496.

[63] B. Stieberova, M. Zilka, M. Ticha, F. Freiberg, P. Caramazana-González, J. McKechnie, E. Lester, *J. Cleaner Prod.* **2019**, *241*, 118325.

[64] M. Pini, R. Rosa, P. Neri, F. Bondioli, A. M. Ferrari, *Green Chem.* **2015**, *17*, 518.

[65] B. M. K. Manda, K. Blok, M. K. Patel, *Sci. Total. Environ.* **2012**, *439*, 307.

[66] N. K. Memon, S. D. Tse, M. Chhowalla, B. H. Kear, *Proc. Combust. Inst.* **2013**, *34*, 2163.

[67] I. Tantis, M. V. Dozzi, L. G. Bettini, G. L. Chiarello, V. Dracopoulos, E. Selli, P. Lianos, *Appl. Catal. B* **2016**, *182*, 369.